Gearbox Instrumentation for the Investigation of Bearing Axial Cracking

Jonathan Keller and Scott Lambert
National Renewable Energy Laboratory

Gearbox Instrumentation for the Investigation of Bearing Axial Cracking

Jonathan Keller and Scott Lambert
National Renewable Energy Laboratory

National Renewable Energy Laboratory
15013 Denver West Parkway
Golden, CO 80401
303-275-3000 • www.nrel.gov

Technical Report
NREL/TP-5000-70639
Revised January 2019

Contract No. DE-AC36-08GO28308

NOTICE

This report was prepared as an account of work sponsored by an agency of the United States government. Neither the United States government nor any agency thereof, nor any of their employees, makes any warranty, express or implied, or assumes any legal liability or responsibility for the accuracy, completeness, or usefulness of any information, apparatus, product, or process disclosed, or represents that its use would not infringe privately owned rights. Reference herein to any specific commercial product, process, or service by trade name, trademark, manufacturer, or otherwise does not necessarily constitute or imply its endorsement, recommendation, or favoring by the United States government or any agency thereof. The views and opinions of authors expressed herein do not necessarily state or reflect those of the United States government or any agency thereof.

Cover Photos by Dennis Schroeder: (left to right) NREL 26173, NREL 18302, NREL 19758, NREL 29642, NREL 19795.

NREL prints on paper that contains recycled content.

Errata

This report, originally published in March 2018, was revised in January 2019. Equations 2, 3 and 4 describing the bearing velocities were updated, along with updates to Figure 7 and associated descriptive text. The discrepancy was caused by a change in the frame of reference for the roller speed measurement. Additionally, minor wording clarifications relating to the roller speed measurements in Figure 27 and 28 were made.

Acknowledgments

List of Acronyms

BB	ball bearing
CRB	cylindrical roller bearing
DC	direct current
GRC	Gearbox Reliability Collaborative
GS-in	inboard generator side
GS-out	outboard generator side
HSS	high-speed shaft
IR	inner ring
kHz	kilohertz
kN	kilonewton
kNm	kilonewton-meter
kW	kilowatt
MW	megawatt
NREL	National Renewable Energy Laboratory
NWTC	National Wind Technology Center
OR	outer ring
rpm	revolutions per minute
RS	Rotor side
RTD	resistance temperature detector
WEC	white-etching crack

Table of Contents

List of Figures

List of Tables

1 Introduction

Failures in gearbox bearings have been the primary source of reliability issues for wind turbine drivetrains, leading to costly downtime and unplanned maintenance [1,2]. The most common failure mode is attributed to so-called axial cracks or white-etching cracks (WECs), which primarily affect the intermediate and high-speed-stage bearings [3]. "Axial" describes the orientation of the crack as it appears on the raceway of the bearing inner ring, in which the direction of the crack is aligned with the axis of rotation of the shaft and bearing inner ring. "White-etching" refers to the appearance of the steel microstructure when the cracked bearing cross-sections are polished, etched with chemicals, and examined under reflected light. These cracks tend to propagate to spalls or lead to a complete splitting of the inner ring. This mode of failure can occur at 5%–20% of the predicted design life and has been observed in many industries, bearing locations, bearing types, bearing components, and steel types [4–6]. Although these types of cracks have been reported for over a decade, the conditions leading to WECs, the process by which this failure culminates, and the reasons for their apparent prevalence in wind turbine gearboxes are all highly debated.

A multipronged research program supported by the U.S. Department of Energy at Argonne National Laboratory and the National Renewable Energy Laboratory (NREL) is examining the causes of WECs in wind turbine gearbox bearings [7]. WECs have been generated on a three-ring-on-roller benchtop test rig in highly loaded sliding conditions. A cumulative frictional energy criteria (E) related to normal load (N), sliding (ΔV), and run time (t) was postulated and can be expressed as [8,9]

$$E = \frac{3}{2} \Delta V \mu N t \tag{1}$$

High-speed-shaft and bearing loads were directly measured and predicted in recent dynamometer testing of a 750-kW wind turbine drivetrain in normal operations, misaligned conditions, and transient events such as braking and grid loss particularly prone to bearing roller sliding [10,11]. However, lacking from the investigation was an actual direct measurement of the bearing roller sliding itself.

If the cumulative frictional sliding energy is the dominant mechanism that causes WECs, understanding the amount of frictional sliding energy that wind turbine bearings are subjected to in typical operations is the next step in the investigation. Therefore, high-speed-shaft and bearing loads and sliding will be measured with a specially instrumented gearbox installed in the General Electric 1.5- MW SLE turbine at the National Wind Technology Center (NWTC). Additional instrumentation will also measure the tribological environment of these bearings, including bearing temperatures, lubricant temperature and water content, air temperature and humidity, and stray electrical current across the bearings. This paper fully describes the instrumentation package compared to prior works [7,12], along with providing examples of data sets acquired in a benchtop setup. Measurements of the meteorological tower, turbine operating environment, and input loads to the gearbox are already routinely captured [13] but are not described in detail here.

2 Test Article and Instrumentation Overview

The test article is a commercial Winergy 4410.4 gearbox installed in the General Electric 1.5 SLE turbine. Similar to previous gearboxes and drivetrains examined by NREL [10,11], the drivetrain is mounted in a three-point configuration, and the gearbox is composed of a single planetary stage followed by two parallel stages with helical gearing. The high-speed shaft for the test Winergy gearbox is supported by NU 232 ECML/L4BC3 and NU 2326 ECML/L4BC3 cylindrical roller bearings (CRBs) on the rotor side (RS) and inboard generator side (GS-in) of the pinion, which together react the radial load from the pinion mesh, and by a QJ 328 four-point contact ball bearing (BB) on the outboard generator side (GS-out) of the shaft, which reacts the axial load from the pinion mesh. A brake disk and the generator coupling are mounted to the outboard portion of the high-speed shaft that protrudes from the gearbox housing. The test gearbox, including an overlay of the high-speed shaft, is shown in Figure 1.
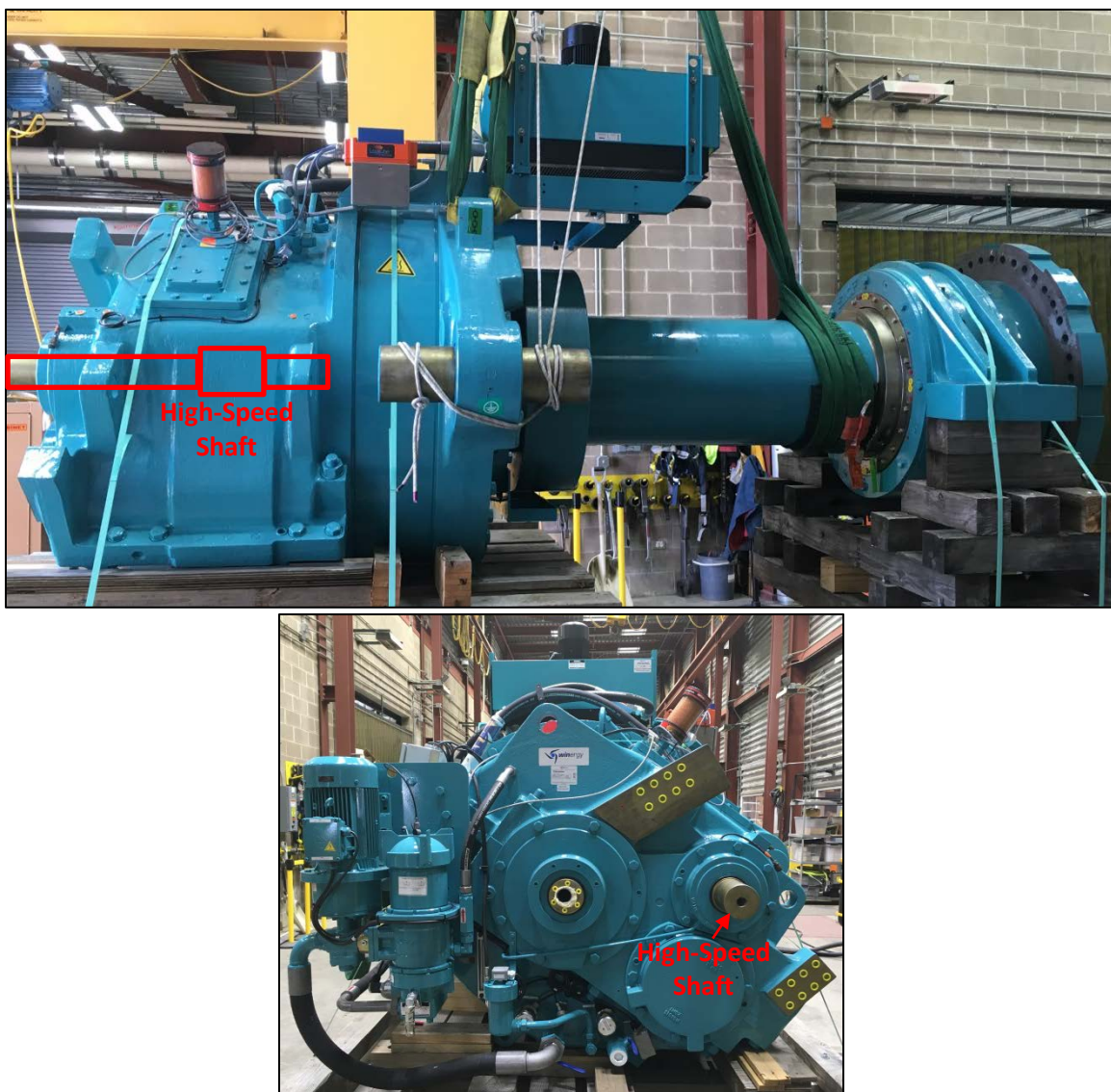
Figure 1. Winergy PEAB 4410.4 gearbox side (top) and rear (bottom) view. *Photos by Jonathan Keller, NREL 49044 and 49045*

2

Of specific interest to the research program is the operational environment of the high-speed shaft and CRBs supporting it. The high-speed-shaft and bearing speeds, shaft torque and bending moments, and tribological environment of the bearings and lubricant will all be measured with an extensive suite of instrumentation inside and outside the gearbox, as shown in Figure 2.
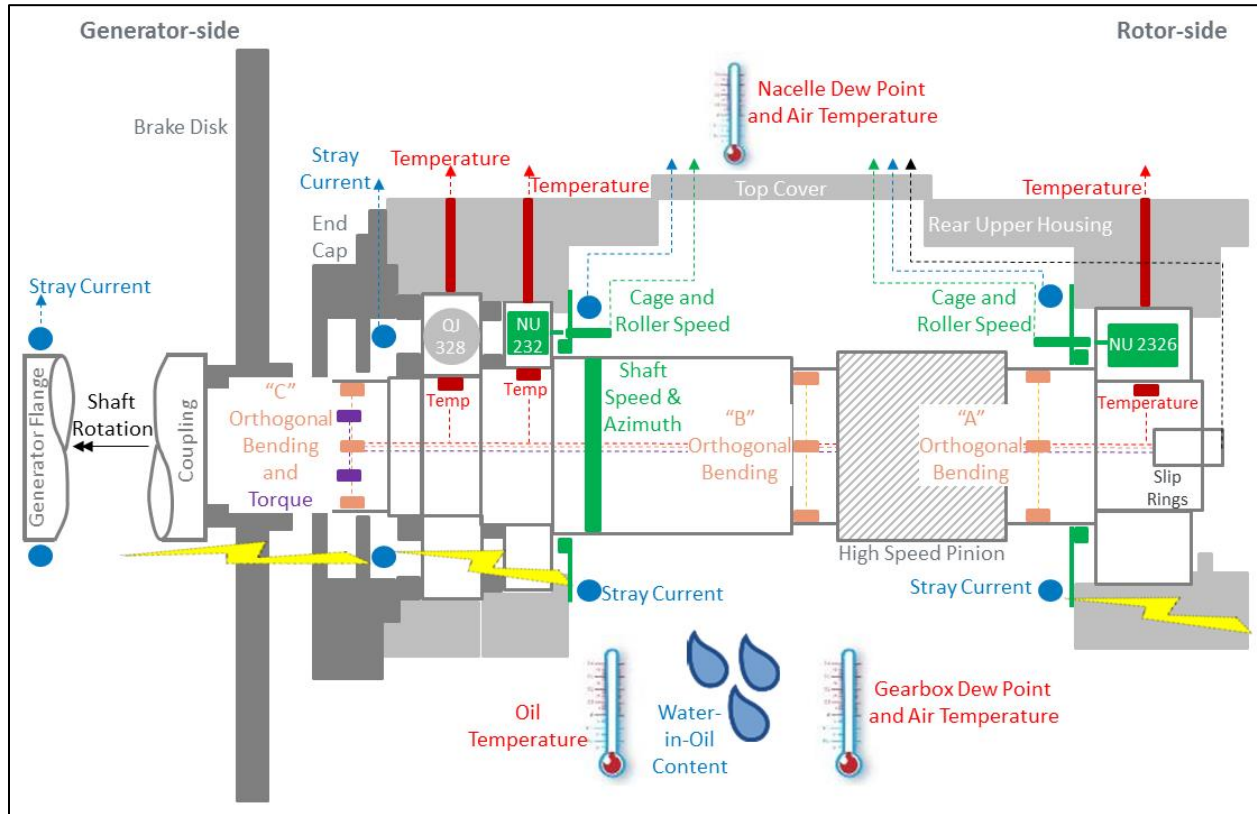
Figure 2. High-speed-shaft instrumentation schematic

To accommodate the instrumentation, the high-speed shaft, rear upper housing, bearing end cap, top cover, and oil distribution manifold were all modified. Most of the modifications were for minor wire routing and attachment, but modifications to the high-speed shaft shown in Figure 3 were extensive to accommodate the instrumentation. The shaft diameter was reduced on either side of the gear teeth and to the rear of the locknut. The wiring for the instrumentation on the high-speed shaft was routed into radial holes to an axial through-hole in the shaft.

Figure 3. Machined high-speed shaft. *Photo by Jonathan Keller, NREL 49040*

The wiring then reached a custom Michigan Scientific SR36M-EL slip ring installed in a counter-bore on the rotor side of the shaft, as shown in Figure 4. The stator of the slip ring was then secured to the gearbox housing with an anti-rotation bracket.

3
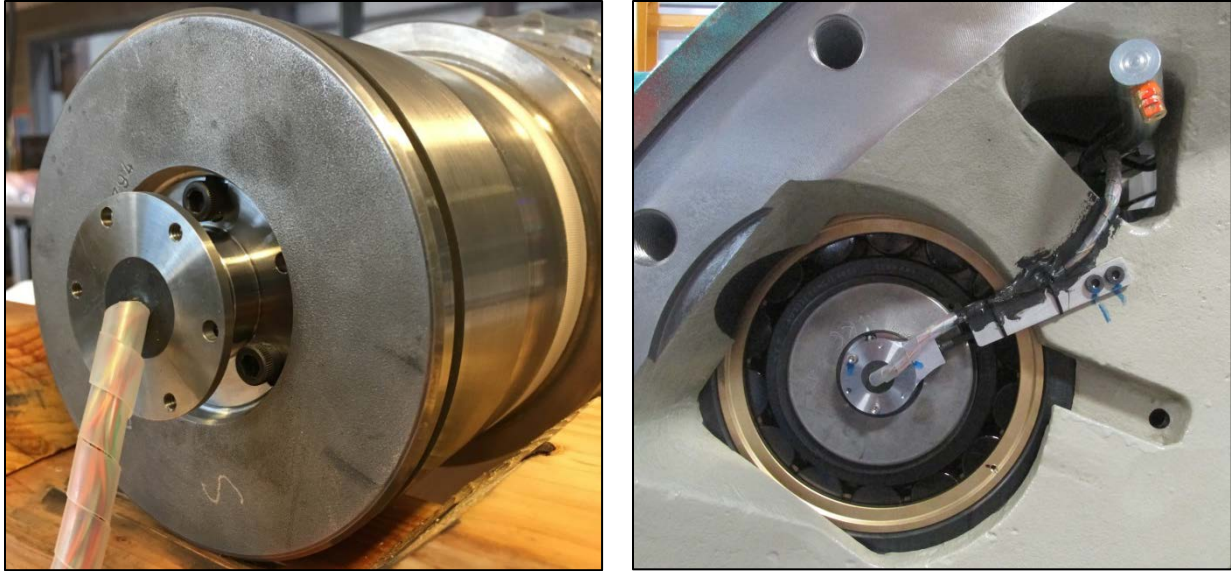
Figure 4. Slip ring (left) and anti-rotation bracket (right). *Photos by Jonathan Keller and Shawn Doner, NREL 49043 and 49752*

The remaining instrumentation was mounted to the rear upper housing, end cap, and oil distribution manifold. All instrumentation and wire routing were designed to accommodate the housing structural features and internal lubrication system, as shown in Figure 5. The internal wiring bundles were then routed to a set of connectors in a bulkhead on the top cover.
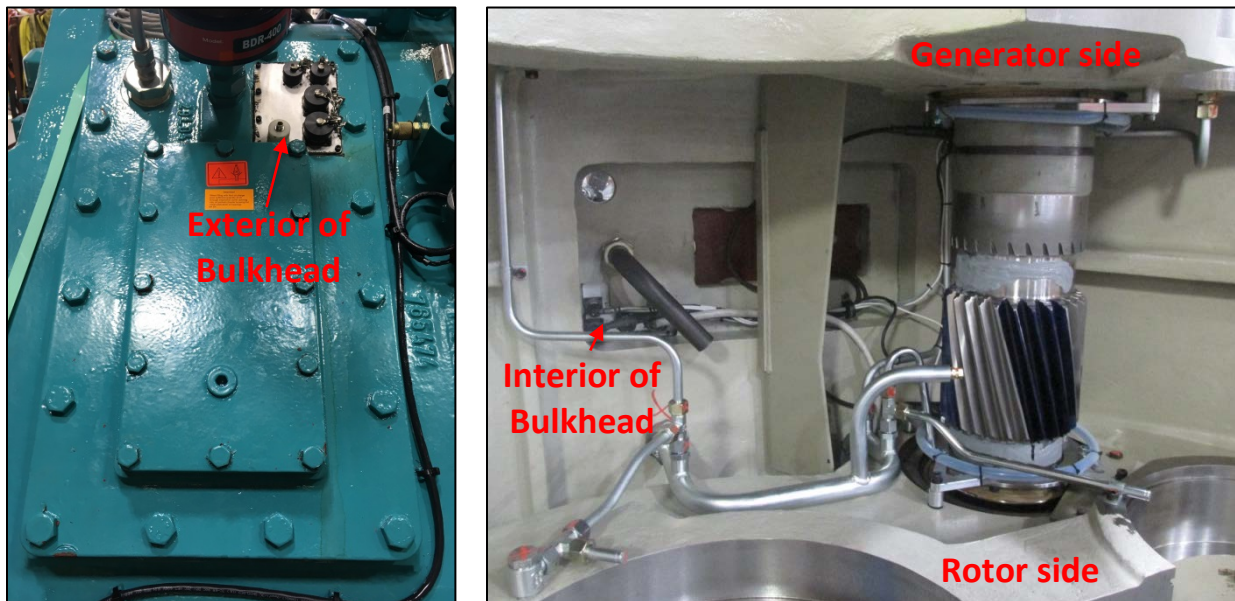
Figure 5. Exterior (left) and interior (right) bulkheads. *Photos by Jonathan Keller and Shawn Doner, NREL 49049 and 49750*

The wiring from the bulkhead and external instrumentation entered a data acquisition enclosure mounted to the right side of the rear upper housing of the gearbox, as shown in Figure 6. Within the enclosure, two National Instruments data acquisition chassis are populated with modules that convert the signals from analog to digital. One Global Positioning System C-Series

4

synchronization module also records all data with the corresponding time for accurate data timestamping and system clock setting, which is especially useful for correlation with the other collected meteorological and turbine operational parameters. The measured data channels are then archived to the NREL network via Ethernet connection.
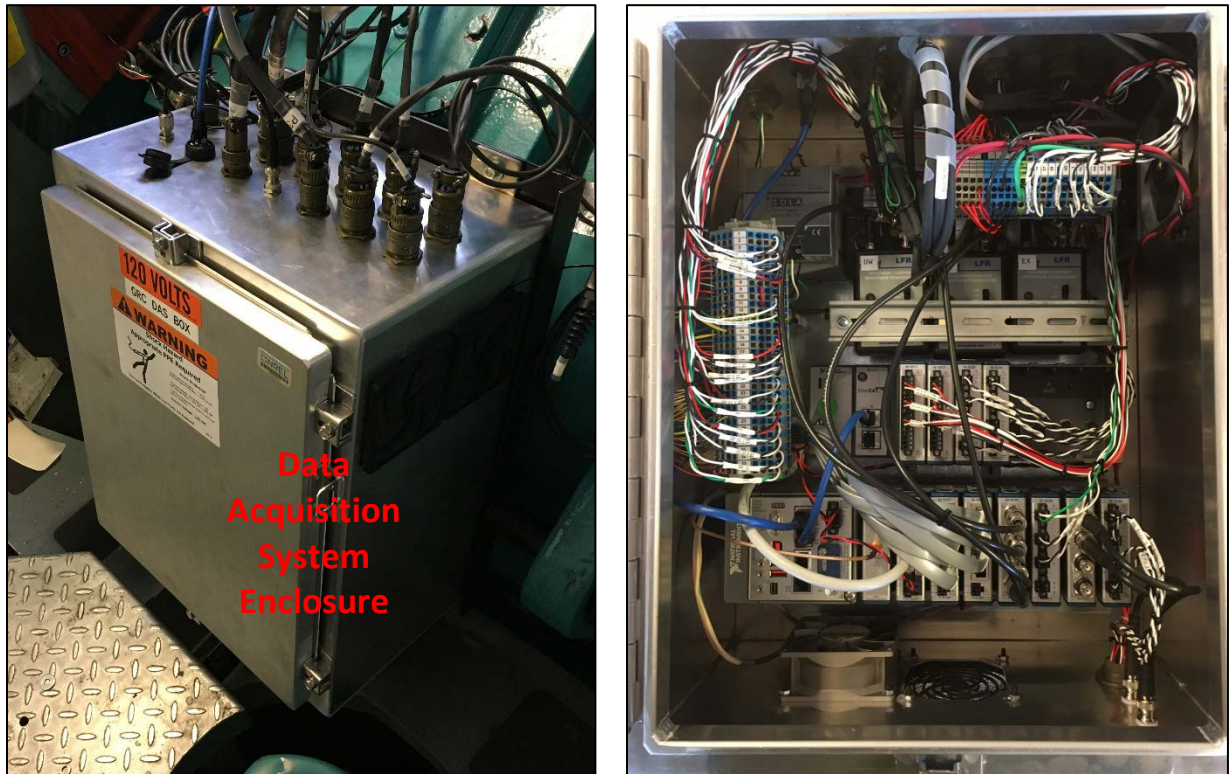
Figure 6. Data acquisition system mounted enclosure (left) and interior view (right). *Photos by Jerry Hur and Jonathan Keller, NREL 49709 and 49046*

3 Instrumentation Description

Each type of instrumentation installed within or on the gearbox is discussed in more detail in the following sections. A full list of the instrumentation devices, measurement units, and rates of acquisition is detailed in Appendix A.

3.1 Shaft and Bearing Speed Instrumentation

Bearing roller sliding can be determined from the combination of the rotational speed of the shaft (ω_s), bearing cages (ω_c), and bearing rolling elements (ω_r) and dimensions of the bearing inner rings and rollers. With these measurements and dimensions, the sliding velocities, as shown in Figure 7, can be determined. The sliding velocity with respect to the inner ring (ΔV_i), which rotates with the shaft, and with respect to the stationary outer ring (ΔV_o) are

$$\Delta V_i = V_i - V_{r_i}$$
$$\Delta V_o = -V_{r_o}$$

(2)

and the inner ring (V_i), cage (V_c), and roller at the inner and roller at the outer ring (V_{r_i} and V_{r_o}) speeds are

$$V_i = \tfrac{1}{2}\,\omega_s F$$
$$V_c = \tfrac{1}{2}\,\omega_c D$$
$$V_{r_i} = V_c - \tfrac{1}{2}\left(\omega_c - \omega_r\right)d$$
$$V_{r_o} = V_c + \tfrac{1}{2}\left(\omega_c - \omega_r\right)d$$

(3)
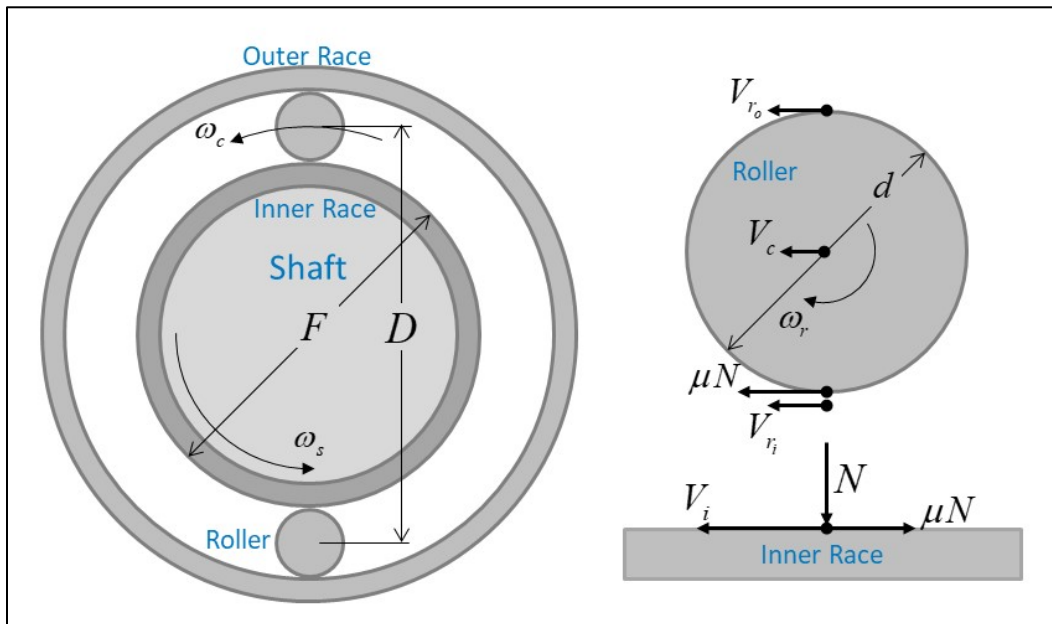
Figure 7. Bearing roller sliding velocities (viewed from generator side)

6

In conditions of pure rolling contact between the rollers and raceways ($\Delta V_i = \Delta V_o = 0$), the velocities in Eq. 3 can be combined and simplified to the well-known equations for the cage and roller rotational speeds in terms of the shaft speed. These theoretical speeds are

$$\omega_c = \frac{1}{2}\omega_s\left(1 - \frac{d}{D}\right)$$
$$\omega_r = \frac{1}{2}\omega_s\frac{D}{d}\left(1 - \frac{d^2}{D^2}\right)$$

(4)

To measure the cage and roller speeds, SKF contributed modified NU 232 ECML/L4BC3 and NU 2326 ECML/L4BC3 CRBs and patented bearing roller speed measurement technology for this project. Standard black-oxide-coated commercial CRBs, shown in Figure 8, were modified by magnetizing one roller and inserting a metal pin in the cage next to it.

Figure 8. NU 232 (left) and 2326 (right) bearings. *Photos by Jonathan Keller, NREL 40979 and 40980*

The relevant parameters for each bearing are listed in Table 1 [14].

Table 1. Bearing Parameters

Quantity	NU 232 ECML/L4BC3	NU 2326 ECML/L4BC3
Number of rollers	19	14
Inner ring diameter, F (mm)	195	167
Pitch diameter, D (mm)	227	207
Roller diameter, d (mm)	32	40

Of all the rotational speeds, by far the most difficult to measure is the rolling element speed. For this measurement, SKF developed and contributed patented instrumentation technology [15].

7

The devices, shown in Figure 9, are purpose-designed inductive coils placed next to each bearing. In operation as the magnetized roller rotates, it generates a change in voltage in the coil that can be measured. The frequency of the measurement is the bearing roller speed (ω_r).

Figure 9. NU 232 (left) and 2326 (right) bearing roller speed instrumentation. *Photos by Jonathan Keller, NREL 40981 and 40982*

Each inductive coil has provisions for mounting it to the gearbox housing with triangular brackets, special cutouts to accommodate lubrication lines and other nearby gearing, and a threaded hole to retain the Allen-Bradley 871TM-N6NN8-J2 proximity switch for the cage speed measurement, as shown in Figure 10. The normal state of the proximity switch is an open electrical setting. But in operation, as the pin on the cage passes the proximity switch, it electrically closes it. The frequency of the closing of the switch is the rotational speed of the cage (ω_c). Additionally, the point in time at which the switch closes determines the azimuthal location of the magnetized roller. Based on the geometries of the rear upper housing and the inductive coils, the NU 232 bearing location is 207.64° and the NU 2326 bearing location is 303.64°, each measured counterclockwise (the same direction of rotation as the high-speed shaft) relative to the vertical direction when viewed from the generator side, as shown in Figure 11. Wiring for the roller speed and cage speed measurements were routed along existing lubrication system piping to the instrumentation bulkhead in the top cover.

Figure 10. NU 232 (left, viewed from rotor side) and 2326 (right, viewed from generator side) bearing cage speed instrumentation. *Photos by Shawn Doner, NREL 49747 and 49748*
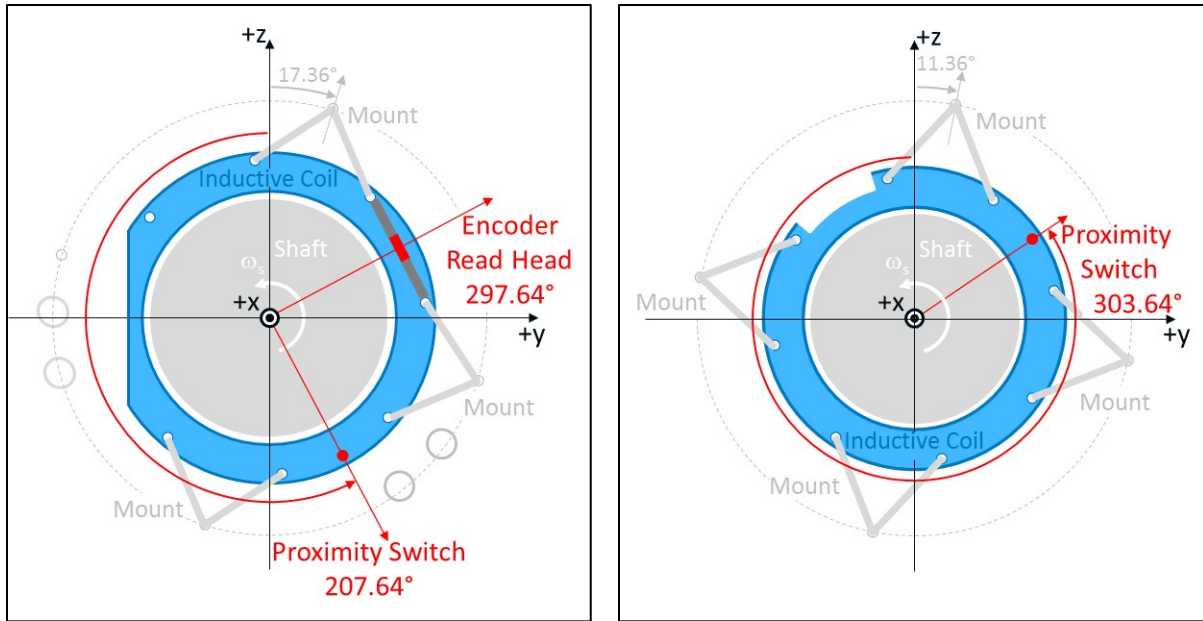
Figure 11. NU 232 (left, viewed from generator side) and 2326 (right, viewed from generator side) proximity switch locations

The final speed measurement is the rotational speed of the high-speed shaft (ω_s). In this case, a Siko MBR320-003 magnetic encoder band was fit over a fiberglass shell on an unmodified section of the shaft, and an MSK320-0987 encoder read head was mounted to the same bracketry as the inductive coils, as shown in Figure 12. The azimuthal location of the encoder read head is 297.64° and is also shown in Figure 11. As the shaft rotates, the instantaneous shaft azimuthal position and speed are recorded relative to the encoder read head. This shaft angular position is required to resolve the bending moments, described in the next section, from the rotating frame to the fixed frame.
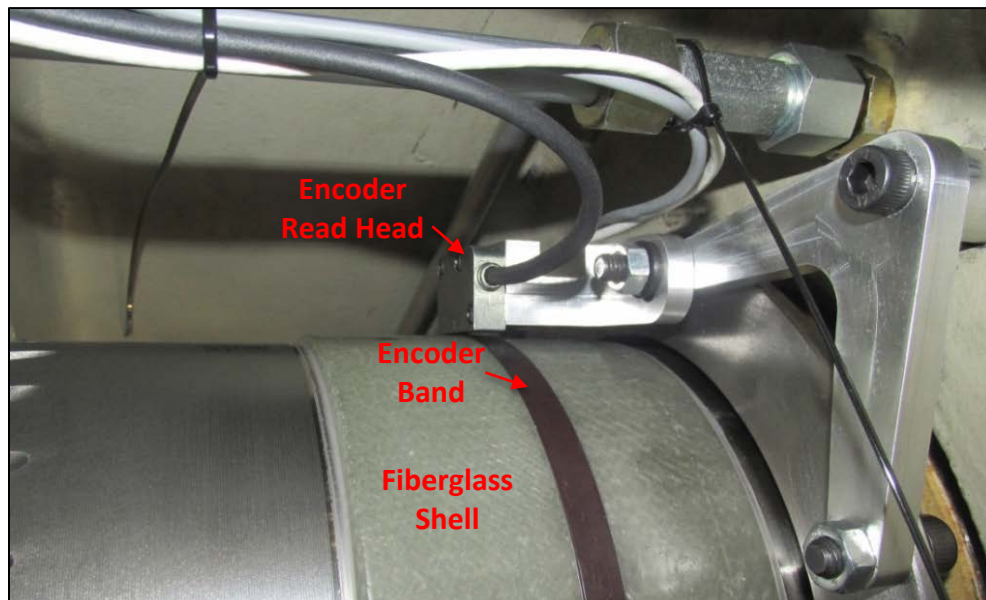
Figure 12. High-speed-shaft speed instrumentation (viewed from rotor side). *Photo by Shawn Doner, NREL 49745*

9

3.2 Shaft Torque and Bending Moment Instrumentation

The next important set of measurements pertains to determining the normal load (N) on the rolling contact. In operation, this load and the resulting contact stress are a function of the shaft torque and related dimensions of the high-speed-shaft and support bearings. As described earlier, the high-speed shaft is supported by three bearings. The two NU-type CRBs and mounting tolerances of the bearing landings are designed to react radial loads from the pinion mesh, while the four-point contact BB and mounting tolerances are designed to react the axial load from the pinion mesh. With this mounting arrangement and similar to previous work [16], the shaft torque, radial loads on each individual CRB, and axial load can be determined with torque and three sets of bending strain gages, as installed on the high-speed shaft shown in Figure 2. To accommodate the instrumentation, the diameter of the high-speed shaft in the area of the load measurements is reduced to increase local strain levels. Strain gages are mounted in full bridge arrangements to measure two orthogonal shaft-bending moments at each of three axial locations along the shaft with Micro Measurements EA-06-125PC-350 type gages and Micro Measurements CEA-06-125UR-350 type gages for shaft torque. Wiring from the strain gage pairs was routed into radial holes to the center of the shaft and then into an axial through-hole to the upwind end of the shaft and terminated at the slip ring assembly. The strain gage pairs on either side of the pinion are shown in Figure 13. All wiring and gages were covered for environmental protection prior to installation in the gearbox.

Figure 13. High-speed-shaft strain gages. *Photos by Jonathan Keller, NREL 49037 and 49033*

High-speed-shaft (HSS) bending moments and torque can be calculated in a manner identical to previous Gearbox Reliability Collaborative (GRC) testing with dimensional and material properties of the shaft and the installed strain gages [17].

$$M = \frac{\pi \left(d_o^{\,4} - d_i^{\,4}\right) E}{32 d_o G_M} \frac{dV}{V} = K_M \frac{dV}{V} \tag{5}$$

$$T = \frac{\pi \left(d_o^{\,4} - d_i^{\,4}\right) E}{16 d_o G_T \left(1 + v\right)} \frac{dV}{V} = K_T \frac{dV}{V} \tag{6}$$

10

The relevant characteristics of the high-speed shaft and instrumentation are listed in Table 2, and the resulting calibration coefficients are listed in Table 3. Negative scale factors relate to particular wiring of the strain gage bridges. The net torque calculated with this process is positive and is in terms of the torque that the HSS applies to the generator.

Table 2. High-Speed-Shaft and Strain Gage Properties

Quantity	Value
A strain gage location from rotor side end of shaft (mm)	174
B strain gage location from rotor side end of shaft (mm)	384
C strain gage location from rotor side end of shaft (mm)	859
Inner diameter, d_i (mm)	20
Outer diameter at A and B strain gage locations, d_o (mm)	157
Outer diameter at C strain and torque gage location, d_o (mm)	130
Modulus of elasticity, E (GPa)	207
Poisson's ratio, v	0.3
Bending gage factor, G_M	2.135
Torque gage factor, G_T	2.15

Table 3. Predicted Shaft Bending and Torque Coefficients

Signal	Calculated Scale Factor (kNm/V/V)
A_Y	-36,830
A_Z	36,830
B_Y	-36,830
B_Z	36,830
C_Y	-20,900
C_Z	20,900
TQ	-31,930

The circumferential location of the strain gage pairs is also specified relative to an angular reset on the Siko MBR320-003 magnetic encoder band, as shown in Figure 14. In the orientation shown, the reported shaft azimuthal position would be 0°; however, the strain gage pairs are offset from this position by 45°. These angular positions are important for resolving the bending moments into the fixed frame.

11
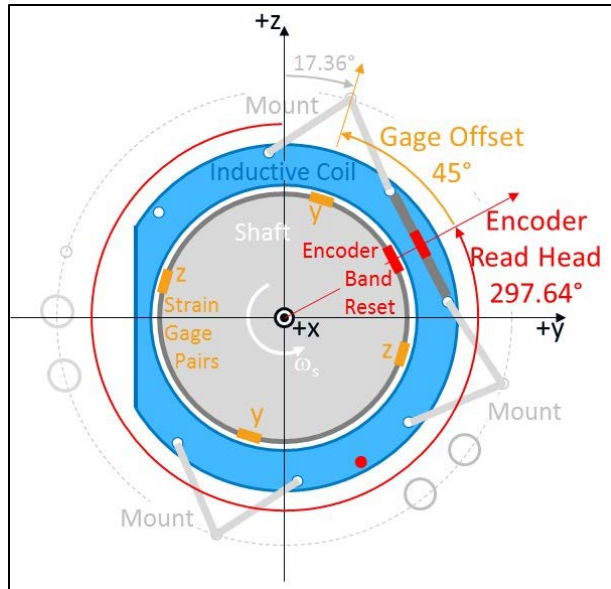
Figure 14. Strain gage circumferential locations (viewed from generator side)

3.3 Environmental Instrumentation

The tribological environment of the bearings is an important factor that can relate to the formation of WECs. This environment includes temperature, humidity, and moisture content and stray electrical current that may result in hydrogen embrittlement or corrosion fatigue cracking.

The temperature, dew point, and humidity of the air within the nacelle and within the gearbox cavity are measured with Vaisala HMP110 C65A1C5B0 sensors. The gearbox cavity sensor was installed on the gearbox top cover next to the instrumentation bulkhead and includes a special protective cap to prevent it from being splashed with gearbox oil. Additionally, the temperature and moisture content of the oil supply to the parallel stages of the gearbox is measured with a Vaisala MMT162 B1BBH0AA70A1X sensor installed in the oil supply manifold. These sensors are shown in Figure 15.
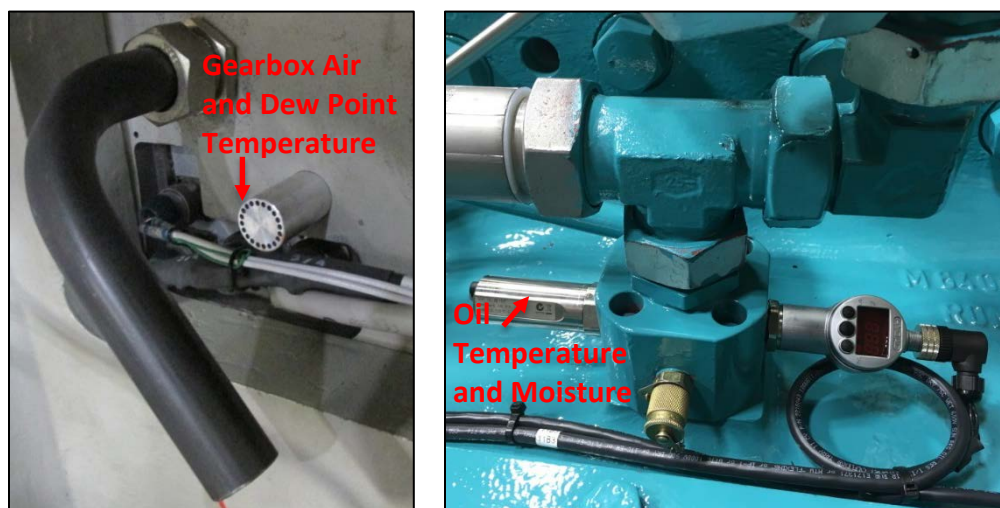
Figure 15. Air and oil lubricant sensors. *Photos by Shawn Doner and Jonathan Keller, NREL 49751 and 49047*

12

Bearing operating temperatures are determined from sensors that are in contact with the bearing rings. The outer ring (OR) temperatures are measured with spring-loaded Burns Engineering resistance temperature detectors (RTDs) that are mounted to the rear upper housing and access the bearings through radial holes. A dual-element Burns 200 B10CN070 RTD is used to monitor the four-point contact BB, and two single-element Burns 200 B10AN070 RTDs are used to monitor the CRBs.

Figure 16. Bearing outer ring temperature sensors. *Photo by Jerry Hur, NREL 49710*

The inner ring (IR) temperatures are measured with Omega RTDCAP-100A-2-P098-050-K-40 temperature sensors that were custom mounted to be spring-loaded against a counterbore in the shaft underneath the bearing landings. The custom spring keeps the RTDCAPs in contact with the inner ring yet allows for some relative movement. The RTDCAPs are then wired through small radial holes to the slip ring. The sensor and spring in Figure 17 are shown as they are being drawn against the counterbore and prior to installation of the inner ring.

Figure 17. Bearing inner ring temperature sensor. *Photos by Jonathan Keller, NREL 49035 and 49036*

13

Stray electrical current is measured with current probes at multiple locations across the high-speed shaft and generator coupling to assess the potential electrical transmission path. A Power Electronics Measurements LFR03/3 B/500 current probe is mounted around the generator coupling to a specially fabricated bracket on the generator output flange, as shown in Figure 18.

Figure 18. Current probe (left) on generator flange (right). *Photos by Scott Lambert, NREL 49051 and 49052*

A second Power Electronics Measurements LFR03/3 B/500 current probe is mounted to the interior side of the modified gearbox high-speed-shaft bearing end cap around the end of the high-speed shaft, as shown in Figure 19. Lastly, two LFR03/3 B/700 current probes are placed around the high-speed shaft and secured to the brackets, which hold the bearing roller speed inductive coils, as shown in Figure 20.
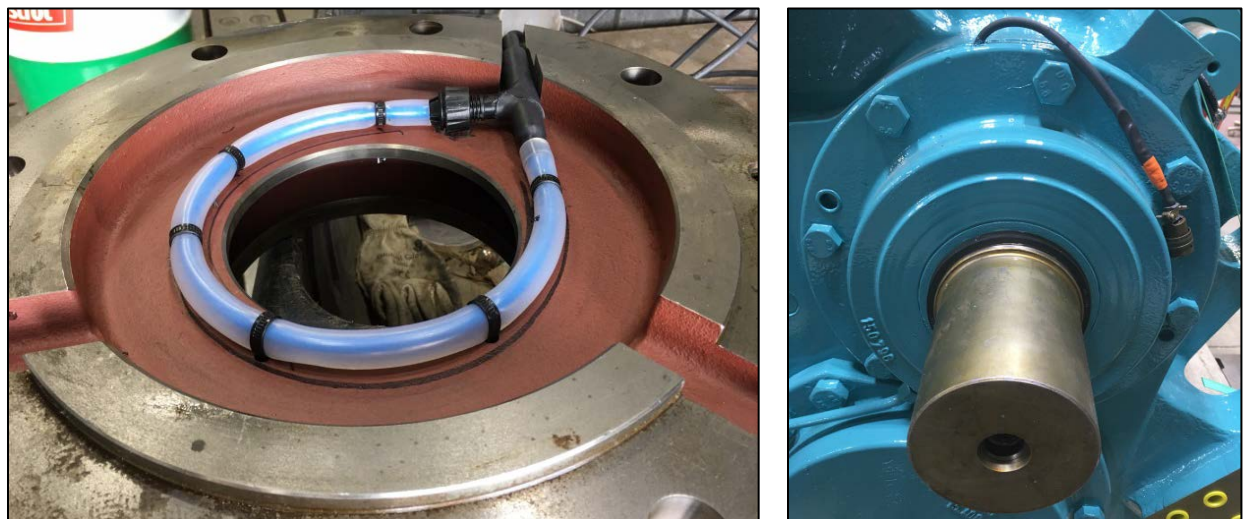
Figure 19. Current probe (left) within bearing end cap (right). *Photos by Jonathan Keller, NREL 49038 and 49048*

14
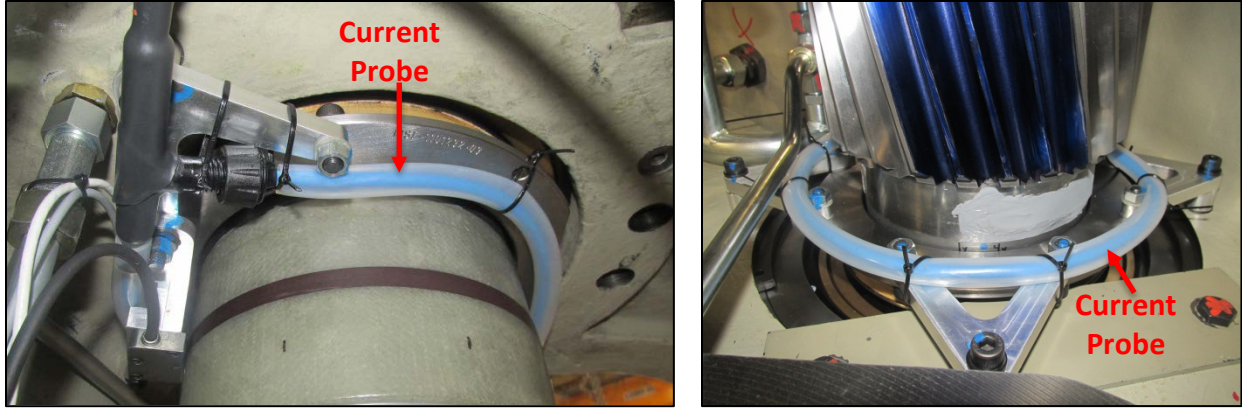
Figure 20. Generator side (left, viewed from rotor side) and rotor side (right, viewed from generator side) current probes. *Photos by Shawn Doner, NREL 49749 and 49746*

Finally, direct current (DC) voltage potential between the high-speed shaft and the rear upper housing is measured. One lead wire is welded to the surface of the high-speed shaft near the upwind side of the gear teeth and then wired through the slip ring. A similar lead wire is welded to the rear upper housing near the upwind bearing. These two lead wires are then routed to the data acquisition system.

4 Initial Testing

The instrumentation package described in the previous section underwent several stages of development and testing prior to installation in the gearbox and fielding in the turbine. This process is described in this section.

4.1 NWTC Bench Testing

A rear upper housing, high-speed shaft, and other associated gearbox parts were modified and assembled together with the modified bearings at the NWTC into a "bench test" stand, as shown in Figure 21, from November 2016 to April 2017. The purpose of this activity was to conduct an instrumentation fit and no-load operational check. Required machining and instrumentation routing challenges were discovered and resolved. A small electric motor was used to spin the high-speed shaft, while recording data from the instrumentation—specifically, the shaft speed, cage speed, and roller speed instruments. Each was confirmed to be working properly in early May 2017. At the conclusion of this process, final machining drawings were developed and released to Winergy in mid-May 2017.

Figure 21. Bench test setup. *Photos by Mark McDade and Jonathan Keller, NREL 49050 and 49041*

4.2 Winergy Load Testing

Machining of the production gearbox parts occurred from June to September 2017, and the second set of modified bearings and roller speed instrumentation were completed in August 2017. NREL and Winergy personnel then assembled the instrumented production gearbox at the Winergy facility in Elgin, Illinois, from September 13–15, 2017. Once completed, a standard production acceptance load test was conducted on the gearbox on September 19, as shown in Figure 22. The load test consisted of an initial flushing of the gearbox, followed by operation at three speed and torque settings up to rated conditions (1,440 rpm, 10.25 kNm, and 1.545 MW) over the course of 3 hours. The gearbox rotational direction is then reversed, and an abbreviated sequence is repeated. The gearbox passed all acceptance test requirements. Data for the instrumentation described in this report were collected during the load test, except for the nacelle air temperature and dew point and generator stray electrical current. These data can be compared

16

to the standard measurements on the production acceptance test equipment for calibration of some data channels and "sanity checking" of others.
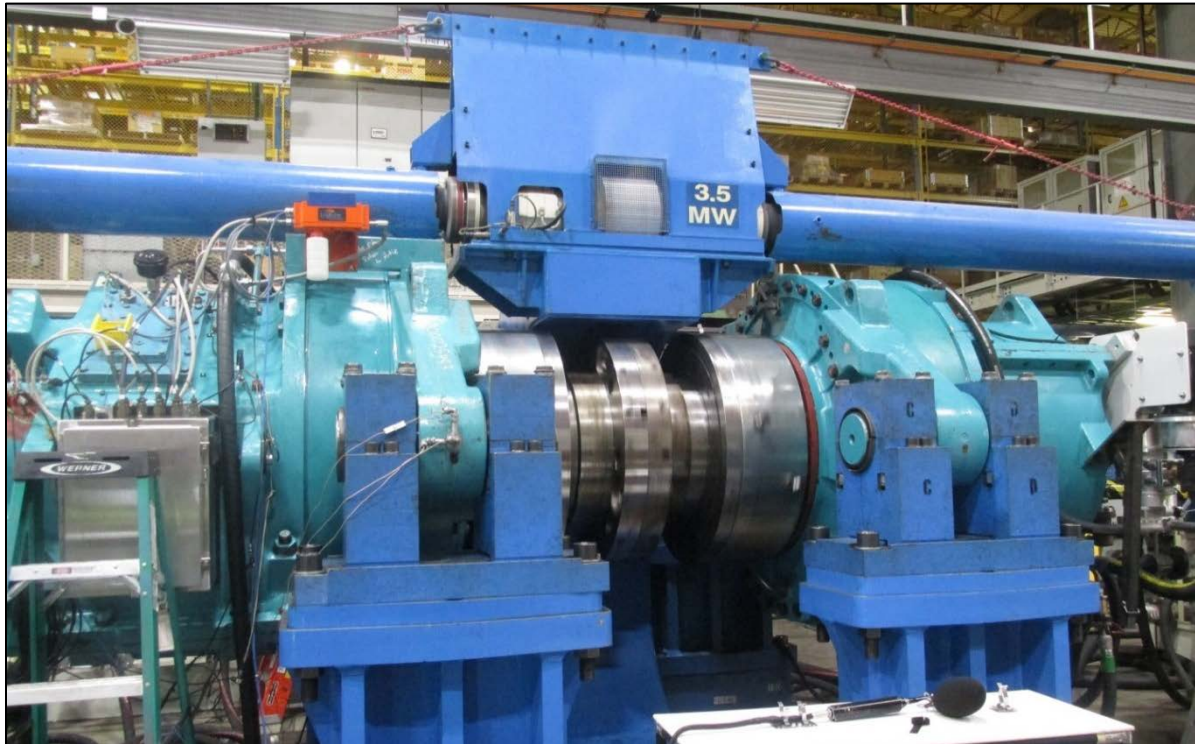
Figure 22. Production acceptance load test. *Photo by Shawn Doner, NREL 50080*

Representative bearing, lubricant, and gearbox air cavity temperatures during the first 3 hours of the load test, with the gearbox operating in the normal rotational direction, are shown in Figure 23. During stationary flushing of the gearbox over the first ½ hour, the bearings, air temperature, and oil temperature were all approximately ambient temperature of 23°C (73°F). The gearbox is then started at 257 kW. Almost as soon as load and speed were applied, the bearing temperatures quickly rise by 10°C (50°F). As the loads and speeds increase further to 600 kW and then rated power, the bearing, lubricant, and air temperatures slowly continue to rise. When the oil supply temperature reaches 60°C (140°F), the oil cooling system engages and quickly cools the oil and drops the bearing temperatures.

17
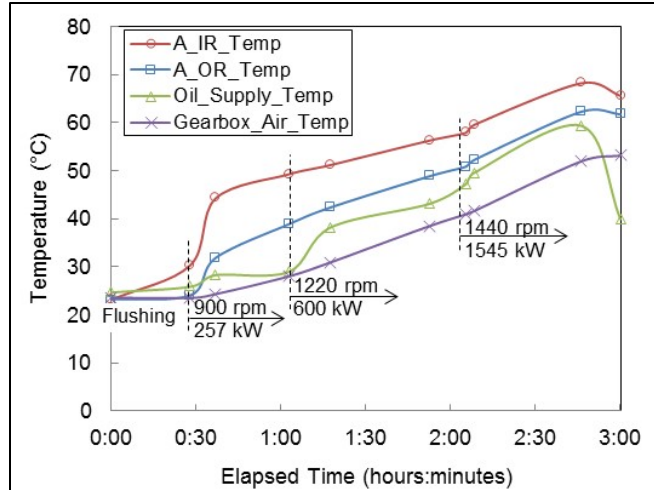
Figure 23. Temperatures during load testing

4.2.1 Shaft and Bearing Speed Results

The cage speed measurements for the rated power and speed condition are shown in Figure 24 over the nearly 8-second acquisition. In this condition, there are almost 80 full revolutions of both bearing cages, or approximately 10 per second. The measured speed of the shaft and hence the theoretical cage speeds predicted by Eq. 4, which assumes pure rolling contact between the rollers and raceway, are nearly constant during the acquisition. The measured cage speeds (ω_c) derived from the proximity switch signals are both within 3 rpm (or 0.5%) of the theoretical cage speeds. The measured cage speed can only be calculated once per revolution, rather than at every point in time, so it is shown as discrete points—each one at the closing of the proximity switch signal. The step values of the measured cage speed are a result of the acquisition rate of 5 kHz.

Figure 24. NU 232 (left) and 2326 (right) cage speeds at rated power

The corresponding bearing roller speed measurements are shown in Figure 25. Similar to the cage speed measurement, the roller speed measurement has only been calculated for each individual roller revolution. Instead of plotting the roller speed over time, the measurements are plotted against the circumferential location of the roller as it travels with the bearing cage and when the roller is at the mid-point of its revolution about its own axis. The orientation of each figure is the same as Figure 11, which is viewed as though standing at the generator side of the

18

gearbox and looking upwind toward the rotor side. In this view, the cages rotate in the counterclockwise direction (the same direction of rotation as the high-speed shaft itself). The radial force exerted by the gear mesh on the high-speed shaft and hence the bearings, ignoring the effect of the weight of the shaft, brake disk, and generator coupling, is almost exactly to the right of the figure ($+y$ or 270°). As seen in the figures, the bearing roller speeds are essentially the same as the theoretical speed near the center of the load zone ($+y$ or 270°). As the rollers leave the load zone near the 330° azimuthal location, they slowly decelerate to about ⅔ of the theoretical value by the time they reach the 180° azimuthal location. Upon re-entering the load zone at approximately 210° azimuth, they quickly accelerate again to the theoretical speed.

Figure 25. NU 232 (left, viewed from generator side) and 2326 (right, viewed from generator side) bearing roller speeds at rated power

The measured cage and roller speeds at rated power can be contrasted to those at a lower power of 257 kW and lower speed of 900 rpm. The cage speed measurements in this condition are shown in Figure 26. Just as before, the measured speed of the shaft and hence the theoretical cage speeds are nearly constant during the acquisition. However, in this case the measured cage speeds (ω_c) are much lower. The NU 232 cage speed is approximately 150 rpm (38%) lower and the NU 2326 is 100 rpm (28%) lower than the theoretical cage speed, suggesting that the rollers are sliding.
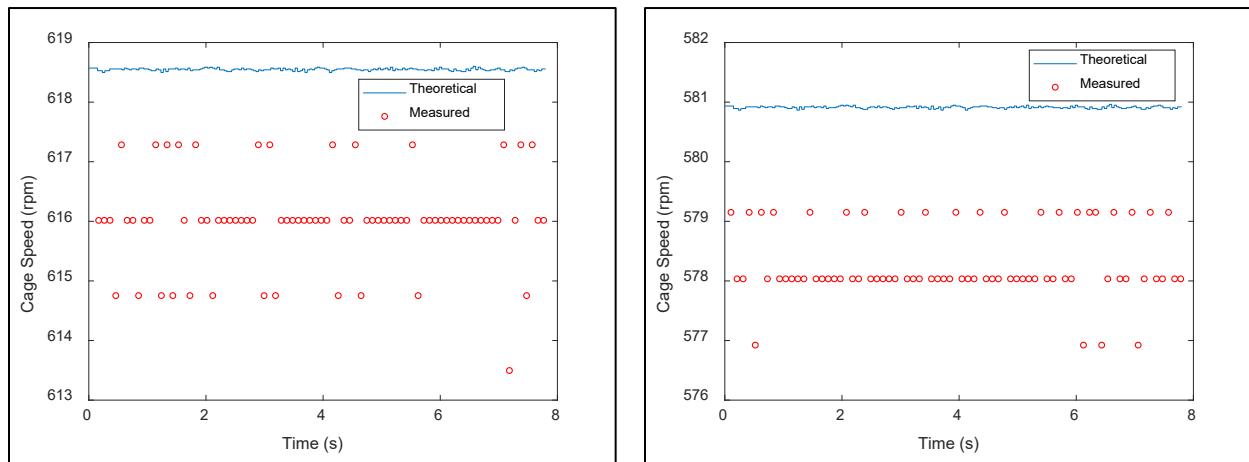
19
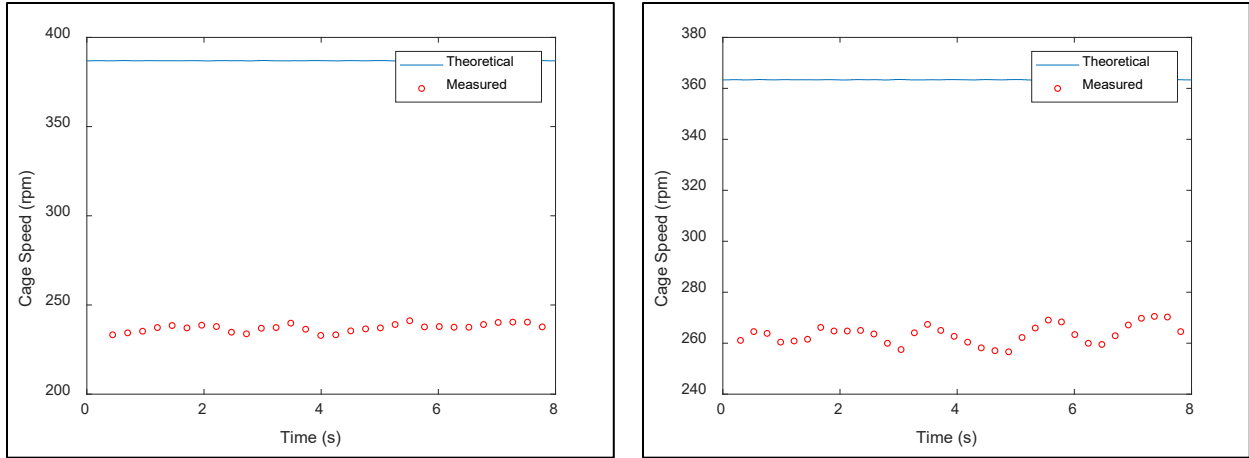
Figure 26. NU 232 (left) and 2326 (right) cage speeds at 257 kW

The corresponding bearing roller speed measurements are shown in Figure 27. Not surprisingly, the bearing roller speeds are also much lower than the theoretical roller speed—even in the center of the load zone. The maximum measured roller speed for the NU 232 is 1,100 rpm (36%) and for the NU 2326 is 750 rpm (29%) lower than the theoretical roller speed. Several factors contribute to this behavior. The torque and resulting bearing radial forces are much lower than at rated power. Additionally, because this condition was performed near the beginning of the load test sequence, both the bearing ring and oil lubricant temperatures are relatively low, resulting in higher viscosity oil.
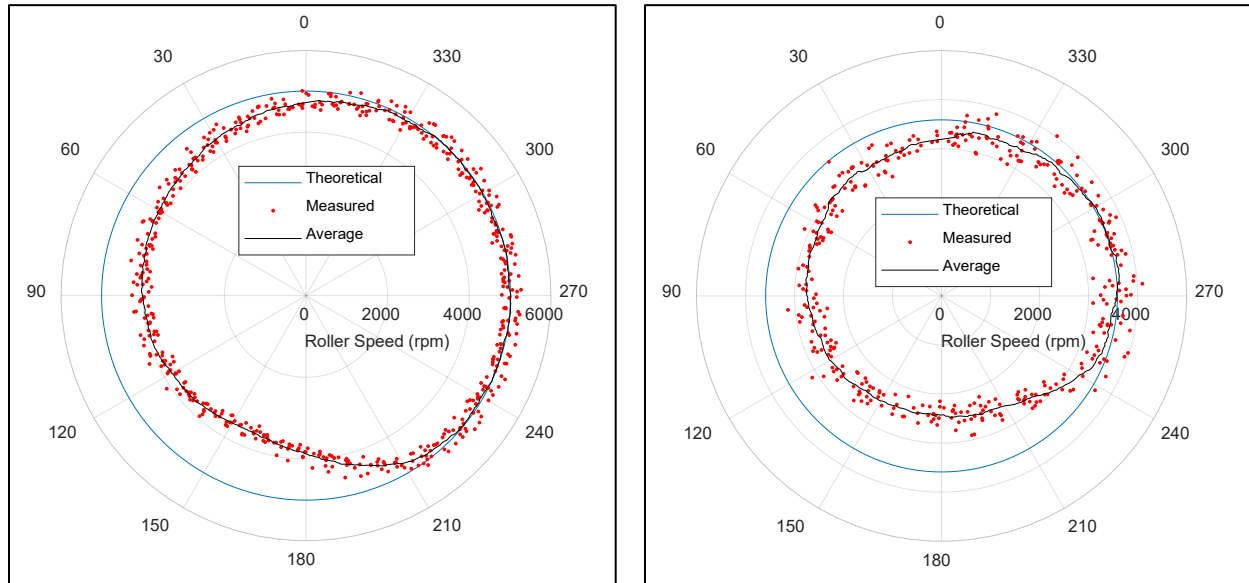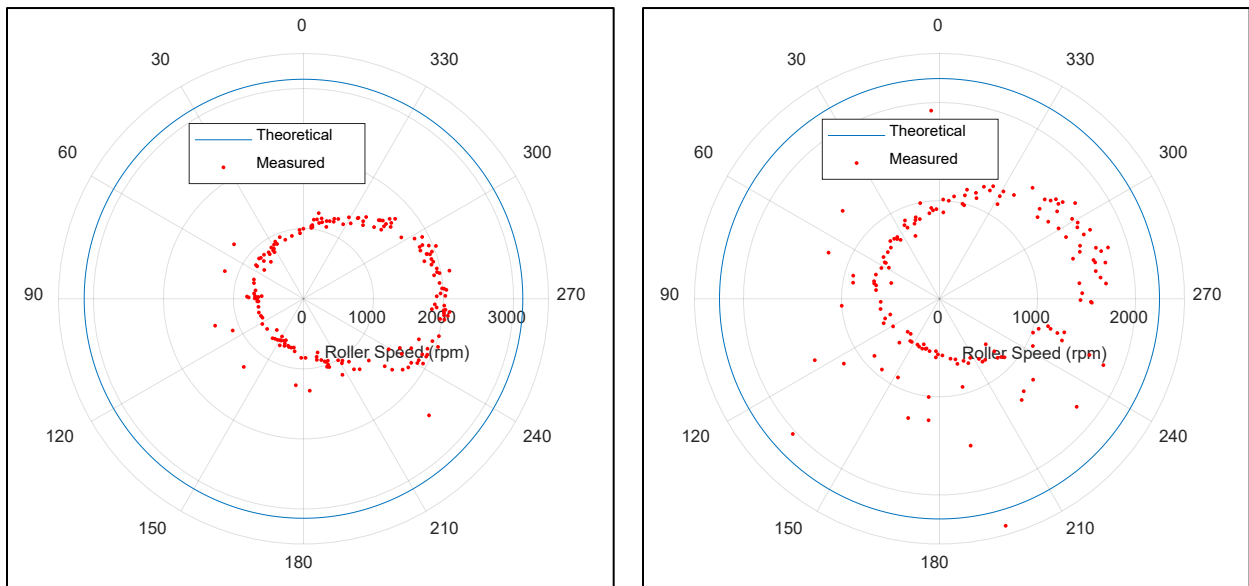

Figure 27. NU 232 (left, viewed from generator side) and 2326 (right, viewed from generator side) bearing roller speeds at 257 kW

Figure 28 shows a summary of the measured cage and bearing roller speeds in terms of the theoretical speed. The profiles are all strikingly similar. With a cold gearbox at low torque and speed, the cage and rolling element speeds are 30%–40% lower than the theoretical values, indicating significant sliding of the rolling elements over the raceways. However, at the middle

20

power setting, the gearbox and lubricant has also warmed appreciably, and the measured speeds are within 5% of the theoretical value.
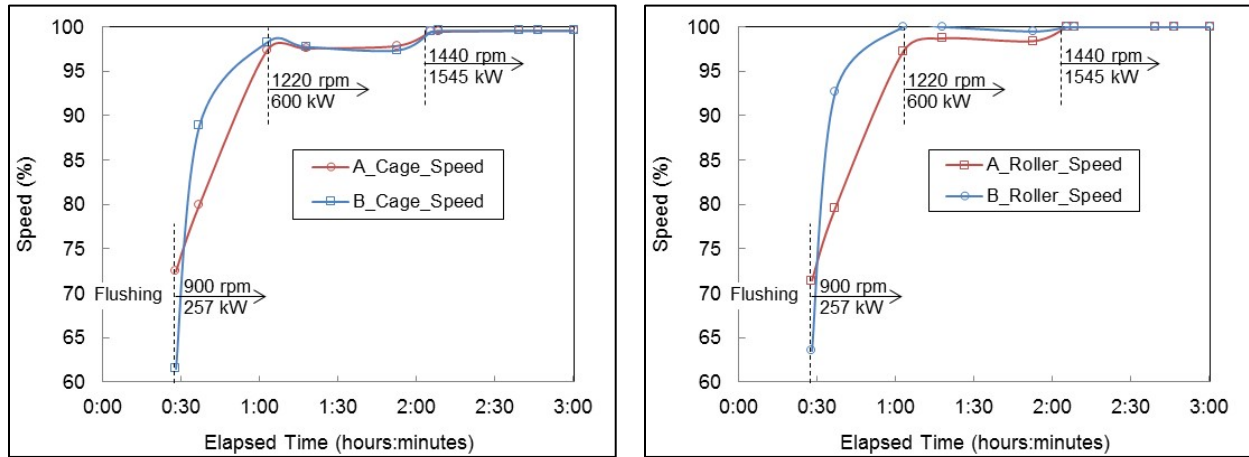
Figure 28. NU 232 and 2326 cage (left) and roller (right) speeds

4.2.2 Shaft Torque and Bending Moment Results

A summary of the measured responses of the shaft torque and bending strain gages over the full range of test stand conditions is shown in Figure 29. The torque response can be compared to the indicated test stand torque as a form of calibration of these strain gages. Two to four acquisitions were taken at each test condition to assess repeatability. The torque measurements were very repeatable—a linear curve fitting approach yields a coefficient of determination (R^2) value over 0.99. The resulting calibration coefficient is -30,838 kNm/V/V, within 4% the analytically derived coefficient of -31,930 kNm/V/V. The static offset of the strain gages was determined from several acquisitions taken while the gearbox was not operating.
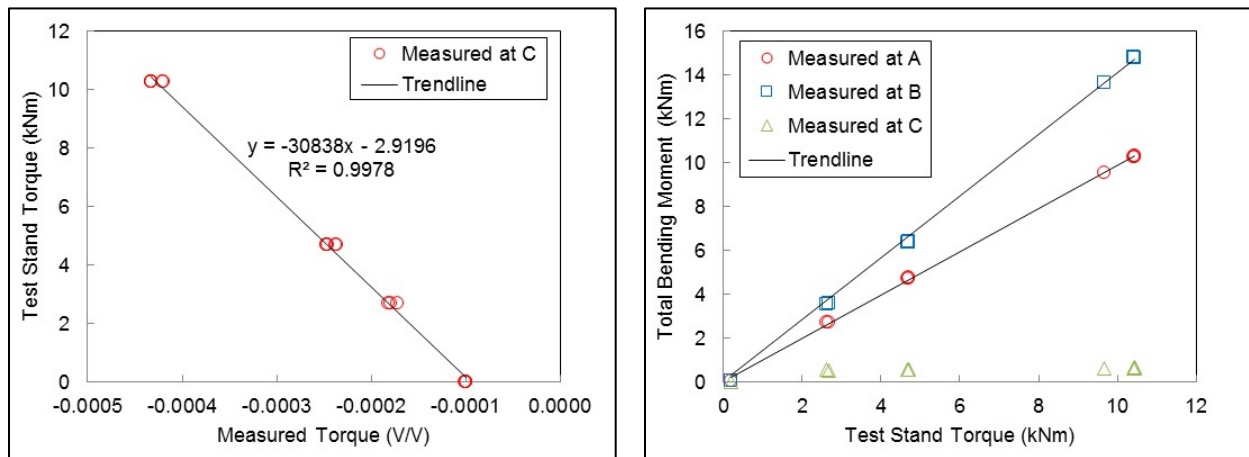
Figure 29. Torque and bending moment data

Although a similar calibration of the bending gages is not possible, the responses of the A and B strain gages on either side of the pinion mesh are expected to increase linearly with torque, as demonstrated in the figure. Comparison of the bending moments with those predicted by a simple shear-moment diagram confirms that the strain gages at location B are expected to have approximately a 30% higher magnitude than at location A. Bending moments ranging from 10 to

21

15 kNm are predicted at these locations at rated torque. At location C, the bending moment is essentially independent of the applied torque. The only bending moment experienced here is a result of the weight-induced moment from the components and any small misalignment-induced moment from couplings and is expected to be less than 1 kNm. Each of these moments was converted from measured to engineering units with the coefficients listed in Table 3 and represent the average of the total magnitude during the acquisition rather than the orthogonal components. The static offset of each strain gage was subtracted out, as the rotating strain gages experience a fully reversing bending moment as a combined effect of the gravity and the gear mesh force, which are stationary in the fixed frame.

5 Summary

Axial cracking or WEC bearing failures continue to have a significant impact on the reliable operation of wind turbine gearboxes, and the root cause of WECs are still a subject of scientific debate. A multipronged research effort by the U.S. Department of Energy is investigating axial crack failures from a material/tribological level to the full-scale system level. This report specifies the instrumentation package that has been installed on a commercial Winergy PEAB 4410.4 gearbox prior to installation in the General Electric 1.5-MW SLE turbine at the NWTC for a measurement campaign. The instrumentation focuses on measuring the operational conditions within the high-speed stage of the gearbox, including shaft torque and loads, bearing sliding, and the tribological environment. Initial results from load testing of the gearbox demonstrate measurements of sliding of the bearing rolling elements, even in steady-state conditions.

References

1. Sheng, S. 2016. *Wind Turbine Gearbox Reliability Database, Condition Monitoring, and Operation and Maintenance Research Update* (Presentation). NREL/PR-5000-66028. National Renewable Energy Laboratory (NREL), Golden, CO (US). http://www.nrel.gov/docs/fy16osti/66028.pdf.

2. Keller, J., S. Sheng, J. Cotrell, and A. Greco. 2016. *Wind Turbine Drivetrain Reliability Collaborative Workshop: A Recap* (Technical Report). DOE/GO-102016-4878. National Renewable Energy Laboratory (NREL), Golden, CO (US). http://www.nrel.gov/docs/fy16osti/66593.pdf.

3. Sheng, S. 2015. *Wind Turbine Gearbox Reliability Database, Condition Monitoring, and O&M Research Update* (Presentation). NREL/PR-5000-63868. National Renewable Energy Laboratory (NREL), Golden, CO (US). http://www.nrel.gov/docs/fy15osti/63868.pdf.

4. Greco, A., S. Sheng, J. Keller, and A. Erdemir. 2013. "Material Wear and Fatigue in Wind Turbine Systems." *Wear*. 302: 1583–1591. doi: 10.1016/j.wear.2013.01.060.

5. Evans, M.-H. 2016. "An Updated Review: White Etching Cracks (WECs) and Axial Cracks in Wind Turbine Gearbox Bearings." *Material Science and Technology*. 32 (11): 1133–1169. doi: 10.1080/02670836.2015.1133022.

6. Gould, B., A. Greco, K. Stadler, and X. Xiao. 2017. "An Analysis of Premature Cracking Associated with Microstructural Alterations in an AISI 52100 Failed Wind Turbine Bearing Using X-ray Tomography." *Materials and Design*. 117: 417–429. doi: 10.1016/j.matdes.2016.12.089.

7. Keller, J., B. Gould, and A. Greco and. 2017. *Investigation of Bearing Axial Cracking: Benchtop and Full-Scale Test Results* (Technical Report). NREL/TP-5000-67523. National Renewable Energy Laboratory (NREL), Golden, CO (US). http://www.nrel.gov/docs/fy17osti/67523.pdf.

8. Gould, B., and A. Greco. 2015. "The Influence of Sliding and Contact Severity on the Generation of White Etching Cracks." *Tribology Letters*. 60 (29). doi: 10.1007/s11249-015-0602-6.

9. Gould, B., and A. Greco. 2016. "Investigating the Process of White Etching Crack Initiation in Bearing Steel." *Tribology Letters*, 62 (26). doi: 10.1007/s11249-016-0673-z.

10. Helsen, J., Y. Guo, J. Keller, and P. Guillaume. 2016. "Experimental Investigation of Bearing Slip in a Wind Turbine Gearbox during a Transient Grid Loss Event." *Wind Energy*. 19 (12): 2255–269. doi: 10.1002/WE.1979.

11. Guo, Y., and J. Keller. 2017. "Investigation of High-Speed-Shaft Bearing Loads in Wind Turbine Gearboxes through Dynamometer Testing." *Wind Energy*. doi: 10.1002/we.2150.

12. Keller, J., D. Vaes, and B. McNiff. 2016. *GRC1.5: Uptower Gearbox Testing to Investigate Bearing Axial Cracking*. NREL/PR-5000-65738. National Renewable Energy Laboratory (NREL), Golden, CO (US). http://www.nrel.gov/docs/fy16osti/65738.pdf.

13. Santos, R., and J. van Dam. 2015. *Mechanical Loads Test Report for the U.S. Department of Energy 1.5-Megawatt Wind Turbine*. NREL/TP-5000-63679. National Renewable Energy Laboratory (NREL), Golden, CO (US). http://www.nrel.gov/docs/fy15osti/63679.pdf.

14. Single Row Cylindrical Roller Bearings. [Online]. http://www.skf.com/us/products/bearings-units-housings/roller-bearings/cylindrical-roller-bearings/single-row-cylindrical-roller-bearings/index.html.

15. Volkmuth, M., K. Stadler, and R. Heemskerk. 2009. "Slippage Measurements in Roller Bearings." Antriebstechnisches Kolloquium, Aachen, Germany.

16. Keller, J., and Y. Guo. 2016. *Gearbox Reliability Collaborative Investigation of High-Speed-Shaft Bearing Loads* (Technical Report). NREL/TP-5000-66175. National Renewable Energy Laboratory (NREL), Golden, CO (US). http://www.nrel.gov/docs/fy16osti/66175.pdf.

17. Keller, J., and B. McNiff. 2014. *Gearbox Reliability Collaborative High-Speed Shaft Calibration* (Technical Report). NREL/TP-5000-62373. National Renewable Energy Laboratory (NREL), Golden, CO (US). http://www.nrel.gov/docs/fy14osti/62373.pdf.

Appendix A. Data Elements

Table A-1. Data Elements

Location	Nomenclature	Expanded Nomenclature	Units	Sensor
DAS	GPS_Time	Time, number of seconds since midnight, January 1, 1904 GMT	s	DAS
RS CRB	A_IR_Temp	Temperature, inner ring of rotor side NU 2326 CRB	°C	Omega RTDCAP-100A-2-P098-050-K-40
RS CRB	A_OR_Temp	Temperature, outer ring of rotor side NU 2326 CRB	°C	Burns 200 B10AN070
RS CRB	A_Cage_Prox	Azimuth indicator, cage of rotor side NU 2326 CRB	-	Allen-Bradley 871TM-N6NN8-J2
RS CRB	A_Cage_Speed	Speed, cage of rotor side NU 2326 CRB	rpm	Calculated
RS CRB	A_Roller_Coil	Speed indicator, roller of rotor side NU 2326 CRB	V	SKF inductive coil
RS CRB	A_Roller_Speed	Speed, roller of rotor side NU 2326 CRB	rpm	Calculated
GS-in CRB	B_IR_Temp	Temperature, inner ring of inboard generator side NU 232 CRB	°C	Omega RTDCAP-100A-2-P098-050-K-40
GS-in CRB	B_OR_Temp	Temperature, outer ring of inboard generator side NU 232 CRB	°C	Burns 200 B10AN070
GS-in CRB	B_Cage_Prox	Azimuth indicator, cage of inboard generator side NU 232 CRB	-	Allen-Bradley 871TM-N6NN8-J2
GS-in CRB	B_Cage_Speed	Speed, cage of inboard generator side NU 232 CRB	rpm	Calculated
GS-in CRB	B_Roller_Coil	Speed indicator, roller of inboard generator side NU 232 CRB	V	SKF inductive coil
GS-in CRB	B_Roller_Speed	Speed, roller of inboard generator side NU 232 CRB	rpm	Calculated
GS-out BB	C_IR_Temp	Temperature, inner ring of outboard generator side QJ 328 BB	°C	Omega RTDCAP-100A-2-P098-050-K-40
GS-out BB	C_OR_Temp	Temperature, outer ring of outboard generator side QJ 328 BB	°C	Burns 200 B10CN070
HS Shaft	HSS_Position	Azimuth, shaft, counts to 14,400	counts	Siko MBR320-003 and MSK320-0987
HS Shaft	HSS_Speed	Speed, shaft	rpm	Calculated

This report is available at no cost from the National Renewable Energy Laboratory at www.nrel.gov/publications.

Location	Nomenclature	Expanded Nomenclature	Units	Sensor
HS Shaft	HSS_Rotation_Count	Total number of rotations since installation, shaft	counts	Calculated
HS Shaft	TQ	Torque, shaft	V/V	Micro Measurements CEA-06-125UR-350
HS Shaft	A_Y	Bending moment, on rotor side of shaft, rotating, y-axis	V/V	Micro Measurements EA-06-125PC-350
HS Shaft	A_Z	Bending moment, on rotor side of shaft, rotating, z-axis	V/V	Micro Measurements EA-06-125PC-350
HS Shaft	B_Y	Bending moment, on generator side of shaft, rotating, y-axis	V/V	Micro Measurements EA-06-125PC-350
HS Shaft	B_Z	Bending moment, on generator side of shaft, rotating, z-axis	V/V	Micro Measurements EA-06-125PC-350
HS Shaft	C_Y	Bending moment, under bearing end cap, rotating, y-axis	V/V	Micro Measurements EA-06-125PC-350
HS Shaft	C_Z	Bending moment, under bearing end cap, rotating, z-axis	V/V	Micro Measurements EA-06-125PC-350
HS Shaft	VDC	Voltage potential, between shaft and housing	V	-
HS Shaft	A_I	Current, shaft rotor side	A	PEM LFR03/3 B/700
HS Shaft	B_I	Current, shaft generator side	A	PEM LFR03/3 B/700
HS Shaft	C_I	Current, in bearing end cap	A	PEM LFR03/3 B/500
Generator	Generator_I	Current, at generator flange	A	PEM LFR03/3 B/500
Oil Supply Line	Oil_Supply_Temp	Temperature, oil supplied to gearbox	°C	Vaisala MMT162 B1BBH0AA70A1X
Oil Supply Line	Oil_Supply_WA	Water activity, oil supplied to gearbox	aw	Vaisala MMT162 B1BBH0AA70A1X
Rear Housing	Gearbox_Air_Dew	Dew point temperature, air inside gearbox cavity	°C	Vaisala HMP110 C65A1C5B0
Rear Housing	Gearbox_Air_Temp	Temperature, air inside gearbox cavity	°C	Vaisala HMP110 C65A1C5B0
Nacelle	Nacelle_Air_Dew	Dew point temperature, air inside nacelle	°C	Vaisala HMP110 C65A1C5B0
Nacelle	Nacelle_Air_Temp	Temperature, air inside nacelle	°C	Vaisala HMP110 C65A1C5B0